Applied Physics A (2024) 130:418
https://doi.org/10.1007/s00339-024-07498-4

Applied Physics A
Materials Science & Processing

Effect of ultrasound irradiation on opto-structural properties and thermal behavior of $Mg(OH)_2$ nanostructures

Sadegh Yousefi[1,2] · Behrooz Ghasemi[1] · Maria P. Nikolova[3] · Cise Unluer[4]

Received: 9 December 2023 / Accepted: 1 April 2024 / Published online: 19 May 2024

Abstract
Magnesium hydroxide ($Mg(OH)_2$) nanoflakes were synthesized by surfactant-assisted sonochemical route with using of natural brine (containing $MgCl_2$), NaOH, and polyethylene glycol as magnesium procedure, precipitator, and surfactant, respectively. The effect of ultrasound irradiation power was investigated in 3 levels (100, 200, and 350 W) on optical, structural, and morphological properties and thermal behavior of as-prepared magnesium hydroxide (MH) nanostructures. XRD, DLS, FESEM, TEM, EDS, FTIR, BET, and UV–visible spectroscopy techniques characterized the synthesized samples. XRD profiles and FESEM and TEM images of all as-synthesized samples disclosed that the $Mg(OH)_2$ nanoflakes indicate hexagonal brucite-type crystallinity with space group P-3m1 without any impurity phases. Also, the crystallite size of samples was increased from 21 to 27 nm by incrementing the ultrasound irradiation power from 100 to 350 W, respectively. Due to the polycrystalline nature of the particles, the size of nanoflakes measured with DLS were 80, 105 and 140 nm for 100, 200, and 350 W irradiation powers, respectively. Well-dispersed $Mg(OH)_2$ nanoflakes with a uniform size distribution were obtained using 100 W irradiation power. Also, FESEM and TEM images confirmed that increasing the ultrasonic wave power led to the accumulation of flakes, which based on BET studies can be due to the reduction of the specific surface area of nanoflakes from 115 m^2/g (for 100 W irradiation) to 35 m^2/g (for 350 W irradiation). The optical band gap energy of the nanoflakes was found to be slightly decreased with increasing with the increase of ultrasound irradiation power content.

Keywords $Mg(OH)_2$ nanoflakes · Ultrasound irradiation power · XRD · TG–DTA · Band gap

1 Introduction

Nanosized metal hydroxides are important engineering materials used in optics, catalysis, photonic, and electronic devices. As a thermally stable, noncorrosive, and nontoxic substance, $Mg(OH)_2$ has been widely utilized as a neutralizer in acid water and treatment of flue-gases (sulfuric oxides), fertilizer additive [1], flame retardant agent [2, 3], energy storage [4], antibacterial [5], anti-acid agents in biomedicine and pharmaceutics [6], remove of heavy metals from water [6], ethanol chemical sensor [7] and a promising candidate for enhanced photocatalytic water splitting in the visible light region [8]. $Mg(OH)_2$ can also be utilized as a raw material for the controlled production of magnesium oxide (MgO) with a well-defined morphology, crystallite size, and surface area [9].

The pollution of water by potentially toxic metals or so-called heavy metals is the most severe form of environmental impact [10]. In recent years, the use of $Mg(OH)_2$ nanoparticles and the composites based on these nanoparticles have attracted the attention of researchers to remove harmful compounds and pollution from water. This potential has been utilized for the degradation of many dangerous compounds such as ciprofloxacin [11], methylene blue dye [12], congo red, malachite green, textile industry effluent [13], rhodamine B, and methyl orange [14]. The mechanism of

✉ Sadegh Yousefi
s.yousefi@semnan.ac.ir

✉ Behrooz Ghasemi
bghasemi@semnan.ac.ir

[1] Department of Metallurgy and Materials Science, Semnan University, Semnan, Iran

[2] Present Address: Ferdows Department of Education (Ministry of Education), Experimental Sciences Teacher, Ferdows, South Khorasan Province, Iran

[3] Department of Material Science and Technology, University of Ruse Angel Kanchev, Ruse 7017, Bulgaria

[4] Department of Solids and Structures, University of Manchester, Manchester M13 9PL, UK

adsorption of toxic metals was proposed in the ion exchange between Mg^{2+} and heavy metals [10]. $Mg(OH)_2$ nanoflakes are one of the more favorable morphologies in the synthesis of $Mg(OH)_2$ nanostructures.

The size, shape, and agglomeration of the hydroxide are crucial for its physicochemical properties and applications. Crystalline $Mg(OH)_2$, referred to as brucite, is known to have a layered crystal structure where successive hexagonal layers of Mg^{2+} ions and OH^- layers are stacked together. This layered structure predetermines its platelet-shaped crystallization [15]. The nanoflakes with edge-on orientation naturally lead to a higher surface-to-volume ratio that is very effective on photocatalytic properties and pollution absorption [12]. In the synthesis of $Mg(OH)_2$ nanostructures, appropriate surfactants significantly reduce size, produce diverse morphologies, and decrease agglomeration of particles [5]. Since the ordered nanostructures are useful in applications like light-emitting diodes, solar cells, and photo-detectors, understanding the optical and thermal characteristics of nanostructures in a controlled synthesis environment can increase their functionality within various applications. The electronic structures of the surfaces of $Mg(OH)_2$ have been calculated by utilizing density functional theory [16]. For all examined (110), (100), (102), (101), and (001) planes, the energy related to the (001) surface was found to be the biggest because of the presence of external OH groups and their low polarity. Moreover, when (110) surface was dominant, the product easily aggregated, while nano-plates with increasing (001) surfaces were much easier to obtain [16–18]. Hexagonal-shaped $Mg(OH)_2$ nanostructures, that possess edge surface atoms, are highly utilizable in biomedical applications because of the presence of edge surface atoms [19].

Although the various synthesis techniques are diverse in form, they are the same in terms of purpose such as optimizing the size and morpho-structural properties of the material to fulfill the necessities of practical application scenarios [20]. Different processes involving chemical precipitation [21], co-precipitation approach [22], hydrothermal synthesis [5], solvothermal reaction [23, 24], water-in-oil microemulsion [25], electrolysis of aqueous magnesium salts [15], spray drying [26], sol–gel techniques [27], chemical vapor deposition (CVD) [28], and ultrasonic methods [29, 30] have been developed for preparation of $Mg(OH)_2$ nanostructures. These nanostructures are conventionally synthesized by precipitation route utilizing magnesium salt solution as magnesium source and utilizing alkali as a precipitant agent. However, there is not enough time for lattice arrangement because of the fast reaction and precipitation rate, resulting in incomplete crystal shape, inconvenient particle size distribution, and aggregation of particles [31].

During the sonochemical synthesis, due to the powerful ultrasound irradiation applied, the molecules undergo a chemical reaction to result in nanoparticles. The acoustic waves create a cavitation field of microbubbles, in which interfacial regions participate in the synthesis reactions taking place at a high pressure (~ 1000 atm), high temperature (~ 5000 K), and rapid heating and cooling [32]. In such extreme conditions, the growth and organization of crystals are hindered, which results in the formation of a nano-sized product. Variation of sonochemical parameters can enable the production of nano-sized particles with distinct sizes and/or morphologies. The sonochemical technique has been utilized to prepare various hydroxide-nanomaterials via a variety of applications and morphological, structural, optical properties, etc. Among these nanomaterials are magnesium hydroxide, aluminum hydroxide [33], calcium hydroxide [34], CoNi layered double hydroxide [35], lanthanum hydroxide [36], nickel hydroxide [37, 38], copper (II) hydroxide nitrate [39], copper-cobalt layered double hydroxide [40], indium(III) hydroxide [41], $Zn(OH)_2/ZnV_3O_8$ [42] and layer-layered double hydroxide [42–44].

Most methods for preparing $Mg(OH)_2$ nanostructures are multi-step and require the presence of other chemicals in the solution, while the ultrasonic method offers oxidation of magnesium in pure solutions [45]. Accordingly, previous studies [30] demonstrated the successful synthesis of highly pure $Mg(OH)_2$ nanostructures from an impure magnesium precursor (i.e. brine) by using a sonochemical route and PEG surfactant. This method is not only fast but also easily controlled, while the products are characterized by their uniform and small sizes. Nevertheless, just a few comprehensive researches on the effect of ultrasound irradiation power in the sonochemical synthesis method on the physicochemical properties of $Mg(OH)_2$ nanostructure can be found in the literature. Accordingly, the present work aims to investigate the effect of ultrasonic wave power on the morphological, structural, optical properties, and thermal behavior of $Mg(OH)_2$ nanostructure. To achieve this, the production of $Mg(OH)_2$ nanostructures by employing controlled sonochemical synthesis that involves the use of different ultrasonic wave intensities (i.e. 100 W (MH-100), 200 W (MH-200), and 350 W (MH-350)) was presented. The composition, structure, morphology, specific surface area, and particle size were investigated to find their role in the thermal and optical properties of the as-synthesized nanostructures.

2 Materials and methodology

2.1 Materials

Natural brine (based on our previous work [46]) containing $MgCl_2$, $CaCl_2$, NaCl, and KCl was utilized as a magnesium procedure for preparing $Mg(OH)_2$ nanostructures. Brine was collected from a solar evaporation pond (Khur Potash

Table 1 The analysis of the used brine as the precursor containing Mg^{2+} ions

Precursor	Concentration (g l^{-1})				Density (g cm^{-3})
	NaCl	KCl	$MgCl_2$	$CaCl_2$	
Brine	5.08	3.62	207.70	507.75	1.43

Complex, Khur-O Biabanak, Isfahan, Iran). The chemical composition of the brine is indicated in Table 1.

Sodium hydroxide (NaOH, purchased from Merck, ≥ 99.99%), absolute ethanol (C_2H_6O, purchased from Merck, ≥ 99.9%), and poly(ethylene glycol) 4000 (PEG 4000, purchased from Sigma-Aldrich) were all analytical reagents and utilized as received, without any purification. For all experiments, high-purity deionized water was produced using deionized water purification equipment (GFL, 2012, Germany).

2.2 Preparation of $Mg(OH)_2$ nanostructures

For each of the experiments, briefly, 50 mL of brine was first transferred into the beaker. Then, 10 mL of PEG4000 solution (5 w.t %) and a certain amount of NaOH solution (3 mol L^{-1}) were mixed for 10 min by a magnetic stirrer to form a uniform solution. Immediately after that, the NaOH/PEG solution was added slowly to the beaker containing brine and simultaneously the ultrasonic irradiation was applied using an ultrasonic homogenizer (UHP 400, Topsonic, Tehran, Iran) with 20-kHz frequency and various powers. Power variations of ultrasound irradiation were made at power intervals of 100, 200, and 350 W and the time duration for all experiments was 15 min. During the reaction of NaOH/PEG solution and brine, small nucleation species appeared, indicating a milky/white solution, and pH was adjusted in the range of 9–9.5. Separation of white $Mg(OH)_2$ precipitates from the mother solution was carried out by vacuum filtration. The obtained cake was washed several times with distilled water and absolute ethanol and dried for 1 h in an oven at 110 °C to obtain $Mg(OH)_2$ powder. The as-synthesized $Mg(OH)_2$ samples at 100 W, 200 W, and 350 W irradiation powers received codes MH-100, MH-200, and MH-350, respectively, and were stored for the next characterizations.

2.3 Characterization

For determining cations (Na^+, K^+, Mg^{2+}, and Ca^{2+}) concentration, flame photometer spectroscopy (for Na^+ and K^+) by JENWAY Flame Photometer and titration method by EDTA (for Mg^{2+} and Ca^{2+}) were used. Moreover, Cl^- concentration was measured through the potentiometric method by JENWAY Ion Meter model 3345.

To appraise the structural properties of as-synthesized MH powders X-ray diffraction (XRD) patterns were recorded using a Bruker X-ray diffractometer (D8 Bruker, CuKα, λ = 1.5406 Å, Germany) at a scan range of 10°–90° 2θ and conditions of 35 kV and 30 mA. The morphology of synthesized $Mg(OH)_2$ nanopowders was analyzed by field emission scanning electron microscopy (FESEM, MIRA3, TE-SCAN) equipped with energy-dispersive X-ray spectroscopy (EDS) and transmission electron microscopy (TEM) using a LEO912-AB microscope. A Malvern NanoZS dynamic light scattering (DLS, ZEN3600) was utilized to determine the size of nanoparticles in an ethanol media at room temperature. Fourier transform infrared (FTIR) spectra were recorded using a TENSOR27 (Germany, Brucker) infrared spectrophotometer with KBr pellets in the range of 400–4000 cm^{-1}. The surface area and pore size studies were performed through a BET (Brunauer–Emmett–Teller) surface area analyzer (Micromeritics ASAP 2020, USA) by N_2 absorption–desorption isotherm curves. Thermal gravimetric and differential thermal analysis and also differential scanning calorimetry (TG–DTA/DSC, VT30-LINSIES) within the range of 25–600 °C were performed at a heating rate of 10 °C/min under air, to characterize the thermal decomposition behavior of the prepared samples. The optical properties of the $Mg(OH)_2$ nanostructures were studied by a diffuse reflection spectrophotometer (DRS, Shimadzu). The absorption spectra were recorded in the range of 195–800 nm.

3 Results and discussion

3.1 XRD and DLS analysis

Figure 1a indicates the XRD patterns of $Mg(OH)_2$ samples synthesized under various ultrasonic wave intensities. XRD patterns illustrate major reflections at 2θ = 18°, 37°, 50°, 58°, 62° corresponding to (001), (100), (101), (102), (110), (111), (103), (201), and (202) crystal planes, which are in good agreement with JCPDS no. 07-0239 for $Mg(OH)_2$ and indicate brucite type hexagonal configuration of all the samples [47]. The presence of sharp and strong XRD peaks illustrates the formation of $Mg(OH)_2$ nanostructures that were well crystallized. No other peaks that could be an indication of impurities were found in the XRD patterns, showing the high purity of the as-synthesized nanostructures. The mean crystallite size (CS) was estimated from the (101) peak and the average of (001), (101), (102), (110), and (111) peaks by using Debye–Scherrer formula (Eq. 1) [48]:

$$D_{CS} = \frac{0.9\lambda}{\beta \cos\theta} \quad (1)$$

where λ is the wavelength of the X-ray, θ is the Bragg angle, 0.9 is a constant near unity, and β is the full width at half-maximum (FWHM). Table 2 reports the average

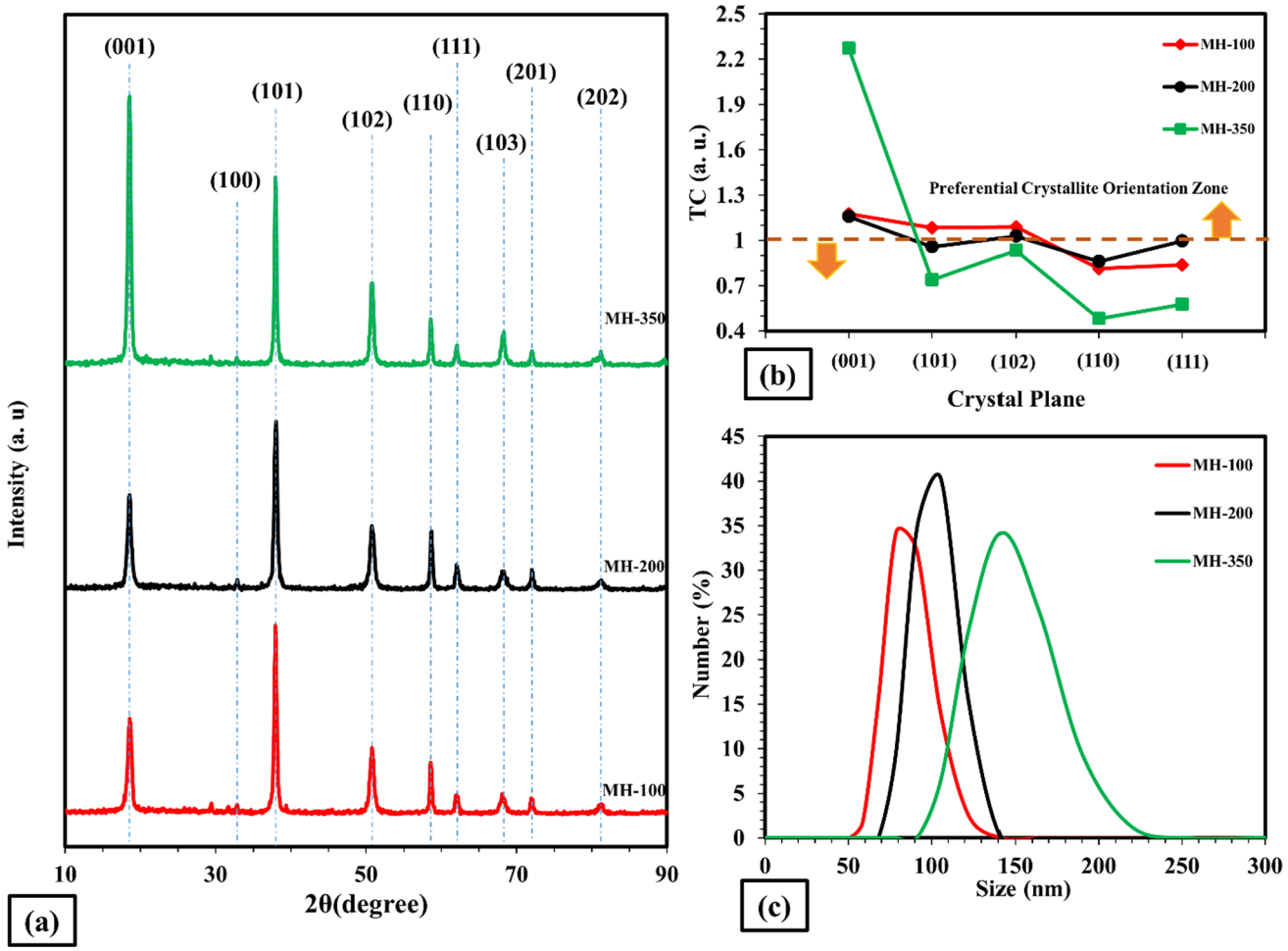

Fig. 1 **a** XRD patterns of $Mg(OH)_2$ nanostructures prepared via ultrasonic under different irradiation powers; **b** effect of ultrasound wave power on texture coefficient (TC) of the as-synthesized $Mg(OH)_2$; and **c** dynamic light scattering (DLS) study of $Mg(OH)_2$ nanostructures

Table 2 Crystallite, particle size, and $I_{(001)}/I_{(101)}$ ratio of as-synthesized $Mg(OH)_2$ obtained by the sonochemical route at different irradiation powers

Sample	Average crystallite size (nm)		$I_{(001)}/I_{(101)}$	Average particle size (nm) (DLS)
	(101)	Average of crystal planes		
MH-100	21.22	18.78	0.57	80
MH-200	22.32	20.35	0.29	105
MH-350	27.46	24.86	0.24	140

crystal sizes of (101) plane, and the average of crystal planes ((001), (101), (102), (110), (111)). The results show that the crystallite size of samples underwent tangible changes by increasing the ultrasound irradiation power. The influence of ultrasound irradiation on the preferential orientation of the crystals was also investigated. The orientation of the crystals in the direction of a particular plane can be estimated by calculating the texture coefficient (TC) of the plane. TC was calculated based on the reflection intensity of different sample planes using the following equation, as shown in Eq. 2 [49]:

$$TC_{(hkl)} = \frac{I_{(hkl)}/I_{0(hkl)}}{\frac{1}{n}\sum_n I_{(hkl)}/I_{0(hkl)}} \quad (2)$$

where TC (hkl) is the texture coefficient, I (hkl) is the (hkl) plane reflection intensity of the sample under analysis, I_0 (hkl) is the reflection intensity of the corresponding plane in the standard card, and n is the number of used peaks (i.e. 5 peaks are considered in this particular case). TC values less than one indicate the random orientation of the plane, whereas TC values greater than one indicate the preferential growth of the plane.

Figure 1b indicates the TC (hkl) values corresponding to different planes of as-synthesized $Mg(OH)_2$ samples. Based

on the information obtained from Eq. (2) and Fig. 1b, it is clear that in all MH samples, the most compact plane in the hexagonal system, namely (001) plane, was the preferred plane for the growth of magnesium hydroxide nanoflakes. Via the simultaneous use of PEG4000 surfactant and increasing the intensity of ultrasonic waves, the crystal orientation in the (001) direction was greatly increased, which led to an increase in the $I_{(001)}/I_{(101)}$ ratio, as shown in Table 2. Alternatively, the orientation of the crystals in (102) direction was blocked. Comparing the I_{001}/I_{101} ratio of the MH samples, the polar nature of crystal face (001) of the MH-350 sample was weaker, which would reduce the internal stress and surface polarity of $Mg(OH)_2$, leading to a more stable structure [50]. Figure 1b also clearly shows that in all specimens, the crystals were not oriented in (110) and (111) direction of planes.

The DLS analysis was used to determine the particle size range of each sample. Figure 1c shows the particle size distribution diagram of $Mg(OH)_2$ samples synthesized under various ultrasound wave power values. The average particle size of the MH-100 sample was revealed as around 80 nm. An increase in the power of ultrasonic waves, due to the increase in the surface energy of the primary nuclei, led to the accumulation of particles, increasing the average particle size and their distribution. Accordingly, the average particle sizes of MH-200 and MH-350 samples reached values of about 105 and 140 nm, respectively. Therefore, to synthesize $Mg(OH)_2$ particles from brine with an average particle size less than 100 nm via the use of a sonochemical method, the device power should not exceed 100 W.

3.2 Morphological and chemical analysis

The morphology of $Mg(OH)_2$ nanostructures was first characterized via FESEM (Fig. 2a–c). It can be seen that all nanopowders revealed plate-like structures that were agglomerated due to their high surface energy. As indicated in Fig. 2, the random agglomerated nanoflakes of $Mg(OH)_2$ were varying in size and thickness containing rice-like nanograins. For MH-100 sample (Fig. 2a), the length and width of the lowest flake were below 50 nm, while the thickness of the lowest flake was about 18 nm. The MH-200 (Fig. 2b) image shows that these nanoflakes have more agglomerated rice-like nanograin, which their boundary was unclear. The MH-350 sample (Fig. 2c) illustrated the most agglomerated rice-like nanograin with a clearer boundary than other samples. So more parallel flakes (via thickness < 25 nm) were detected in the microscopic images for this sample. With an increase in the power of irradiation, the samples turned into smooth semi-plates and seeds, as observed in the FESEM images.

For the further characterization of the morphology of $Mg(OH)_2$ nanoparticles, TEM analysis was carried out. As the power of ultrasonic waves increased, the accumulation of flakes was enhanced, as shown in Fig. 3(a-d). The most random flakes containing agglomerated rice-like nanograins were observed in the MH-350 sample (Fig. 3d). Furthermore, the changes in the arrangement of $Mg(OH)_2$ nanoflakes and the formation of uniform and smooth semi-plates have greatly reduced the available pores, leading to relatively dense morphologies. Amongst the samples investigated, the MH-100 sample revealed a fine nanostructure with a relatively narrow particle size distribution (Fig. 3a, b), which was associated with the use of the lowest ultrasound device power of 100 W.

Overall, the findings obtained by DLS, FESEM, and TEM analyses were in line with each other, revealing the conditions used in the synthesis of the MH-100 sample as ideal for obtaining $Mg(OH)_2$ nanoflakes with the most homogeneous and uniform particle size distribution.

To study the chemical composition of the samples, EDS spectra were recorded together with the FESEM analysis, as shown in Fig. 4. In all the spectra, only Mg and O were detected and no other impurities were detected (i.e. except for Au, which was related to the sample coating) indicating the purity of the synthesized products. The carbon peak observed in all samples was associated with the absorption of PEG 4000 on the sample surfaces during the synthesis. Based on stoichiometric calculations, $Mg(OH)_2$ contains 55.17 wt% oxygen and 41.73 wt% magnesium. The difference in the amounts of oxygen and magnesium from these corresponding stoichiometric values was because of the hydrophilic nature of the $Mg(OH)_2$ nanostructure. Accordingly, this mineral substance can easily absorb moisture from the ambient atmosphere in the form of surface water, which could alter its stoichiometric composition [51]. Nevertheless, the EDS data were in good agreement with the XRD results, indicating the high purity of synthesized MH nanostructures.

The simultaneous use of PEG 4000 surfactant as a capping agent during ultrasonic irradiation led to a more uniform arrangement and clustering of nanoflakes. This surfactant can be adsorbed at the crystal plane of $Mg(OH)_2$, either by hydrogen bonding with the OH groups associated with Mg^{2+} atoms or by coordination with Mg^{2+}, respectively. The adsorption of the PEG molecules blocks the growth of the crystals, resulting in the formation of plate-like particles and also preferential growth in special directions [46].

The surfactant ultrasound-assisted $Mg(OH)_2$ nanostructures from brine according to **Yousefi's model** can be described by the following reactions and steps [52, 53]:

$$MgCl_2(\text{in brine}) \rightarrow Mg^{2+} + Cl^- \tag{3a}$$

$$Mg^{2+} + OH^-(NaOH) \rightarrow Mg(OH)^+ \left(\text{or } \left[Mg(OH)_6\right]^{4-}\right) \tag{3b}$$

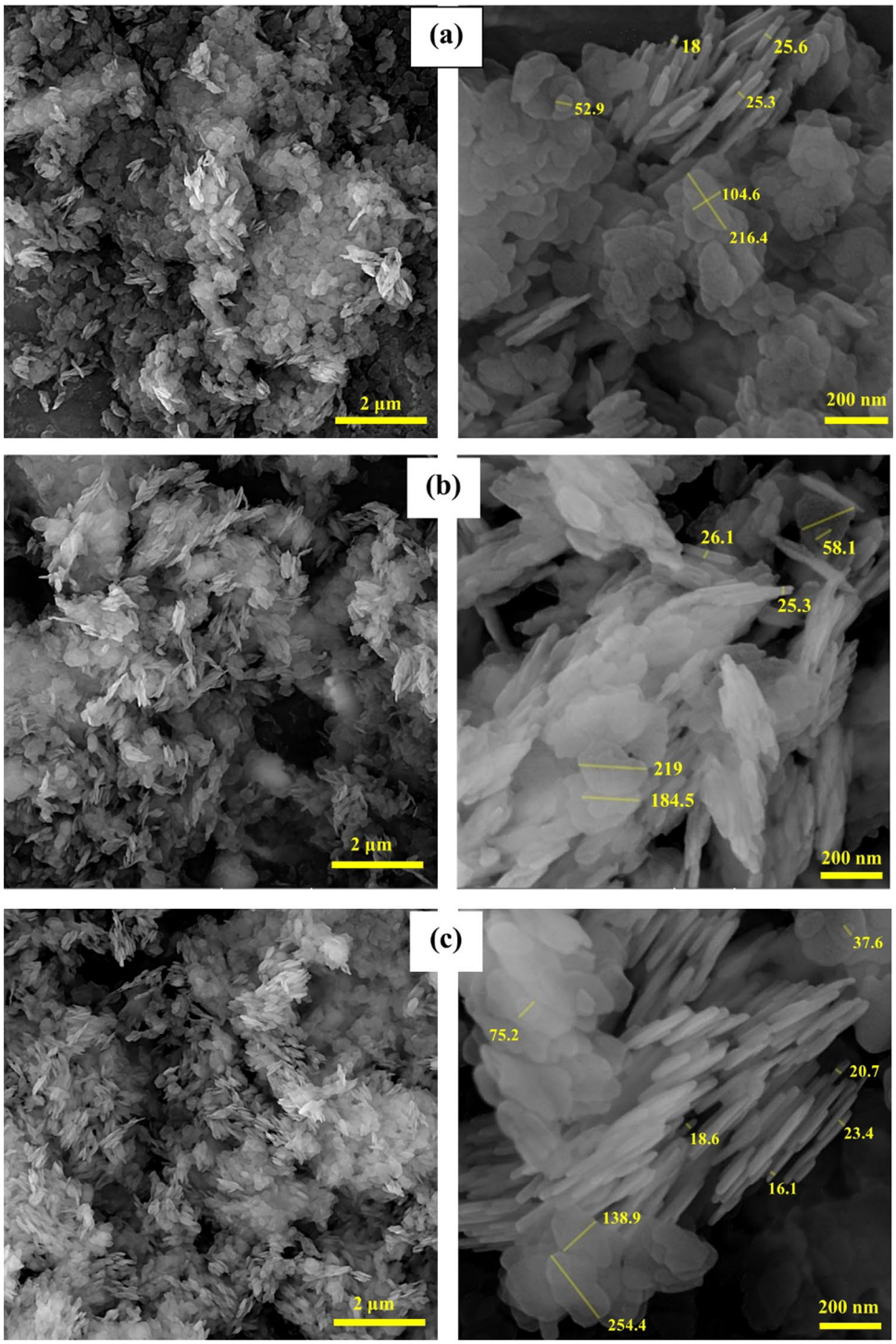

Fig. 2 FESEM images of $Mg(OH)_2$ nanostructures prepared via ultrasonic irradiation under different irradiation powers: **a** MH-100 sample; **b** MH-200 sample; and **c** MH-350 sample

$$Mg(OH)^{+}\left(\text{or } \left[Mg(OH)_6\right]^{4-}\right) + OH^{-}(NaOH) \rightarrow Mg(OH)_2 \quad (3c)$$

$$Mg^{2+} + 2OH^{-}(NaOH) \rightarrow Mg(OH)_2 \quad (3d)$$

$$OH - Mg - OH + H - \left(O - CH_2 - CH_2\right)_n \rightarrow HO - Mg - \left(O - CH_2 - CH_2\right)_n OH \quad (3e)$$

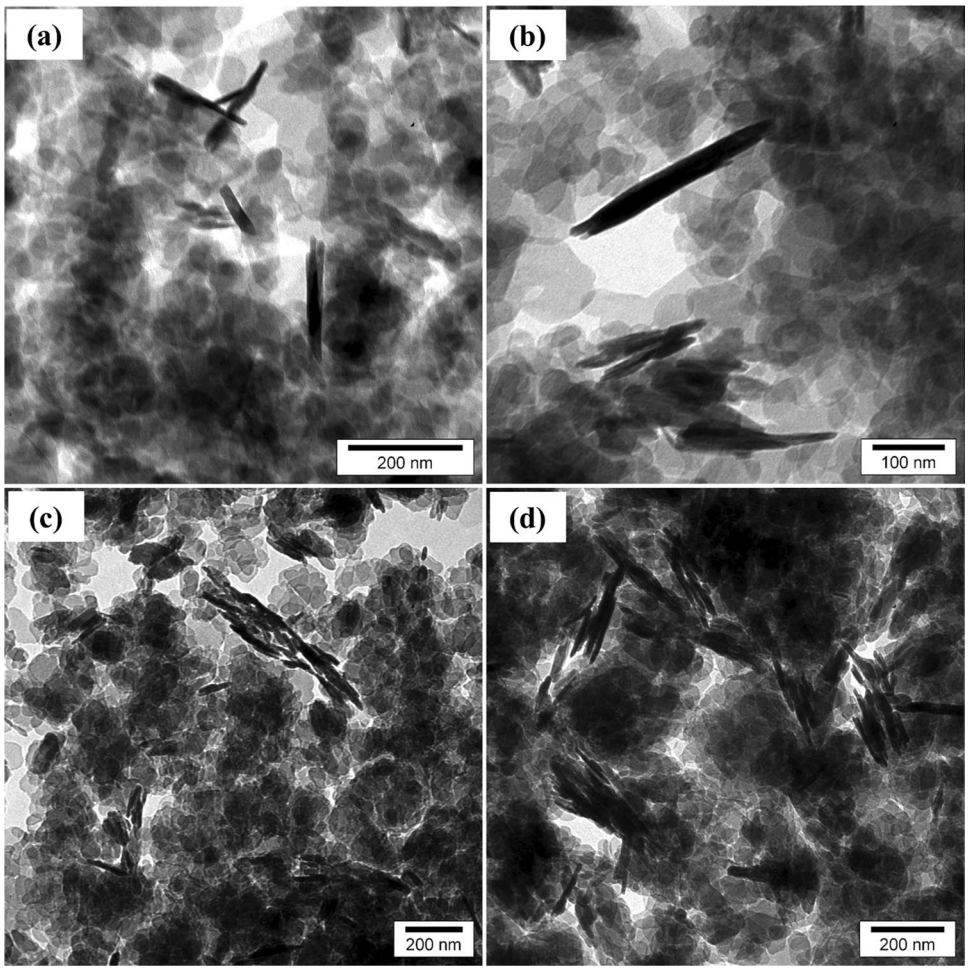

Fig. 3 TEM images of $Mg(OH)_2$ nanostructures prepared via ultrasonic irradiation under different irradiation powers: **a**, **b** MH-100; **c** MH-200; and **d** MH-350

The growth unit of $Mg(OH)_2$ nanostructures has usually been explained by $Mg(OH)^+$ or $[Mg(OH)_6]^{4-}$ species. In the presence of NaOH and PEG, solution, Mg^{2+} ions (in brine) reacted with hydroxyl ion (from NaOH) to form $Mg(OH)^+$ (or $[Mg(OH)_6]^{4-}$) under alkaline condition. In the first stages of the reaction, these small entities act as the primary nuclei of $Mg(OH)_2$.

During the reaction of Mg^{2+} and hydroxyl ions, the OH^- ions are preferentially adsorbed on the Mg^{2+}-terminated (001) plane. High OH^- ion will generate more $Mg(OH)^+$ (or $[Mg(OH)_6]^{4-}$) intermediate, which is also absorbed on Mg^{2+}-terminated (001) plane, which impeded the crystal growth along the c-axis. The use of PEG surfactant (while adding the precipitating agent) blocks the growth along the (001) plane. But in sample MH-350, due to the increase in the power of the ultrasonic waves, the effect of this surfactant will be neutralized and the preferential growth will continue along the plane (001) and cause the agglomeration of $Mg(OH)_2$ nanoflakes. The $Mg(OH)_2$ crystal growth mechanism by surfactant-assisted sonochemical method has been proposed in Fig. 5.

3.3 FTIR and surface area analysis

The possible interactions between PEG 4000 and $Mg(OH)_2$ nanoparticles were further explored by FTIR spectroscopy, whose results are demonstrated in Fig. 6. The details of all the observed absorption bonds, their intensity, and type of vibrations, due to the subsequent vibrations of the different functional groups [54], are listed in Table 3. The absorption vibrations of PEG 4000 groups could be observed in all $Mg(OH)_2$ samples. In line with the XRD and EDS findings, the FTIR spectra indicated the high purity of the synthesized nanostructures. Also, as it is clear, increasing the power of ultrasonic waves has not much effect on the appeared peaks in the FTIR spectra and different functional groups.

The typical N_2 adsorption–desorption isotherms of the synthesized $Mg(OH)_2$ samples are illustrated in Fig. 7. The nitrogen adsorption profiles of all samples could be classified as type-IV with H3 hysteresis loop according to the IUPAC standard, which was associated with slit-like pores [65]. This type of hysteresis corresponds to solids comprising accumulates or agglomerates of particles with slit-shaped

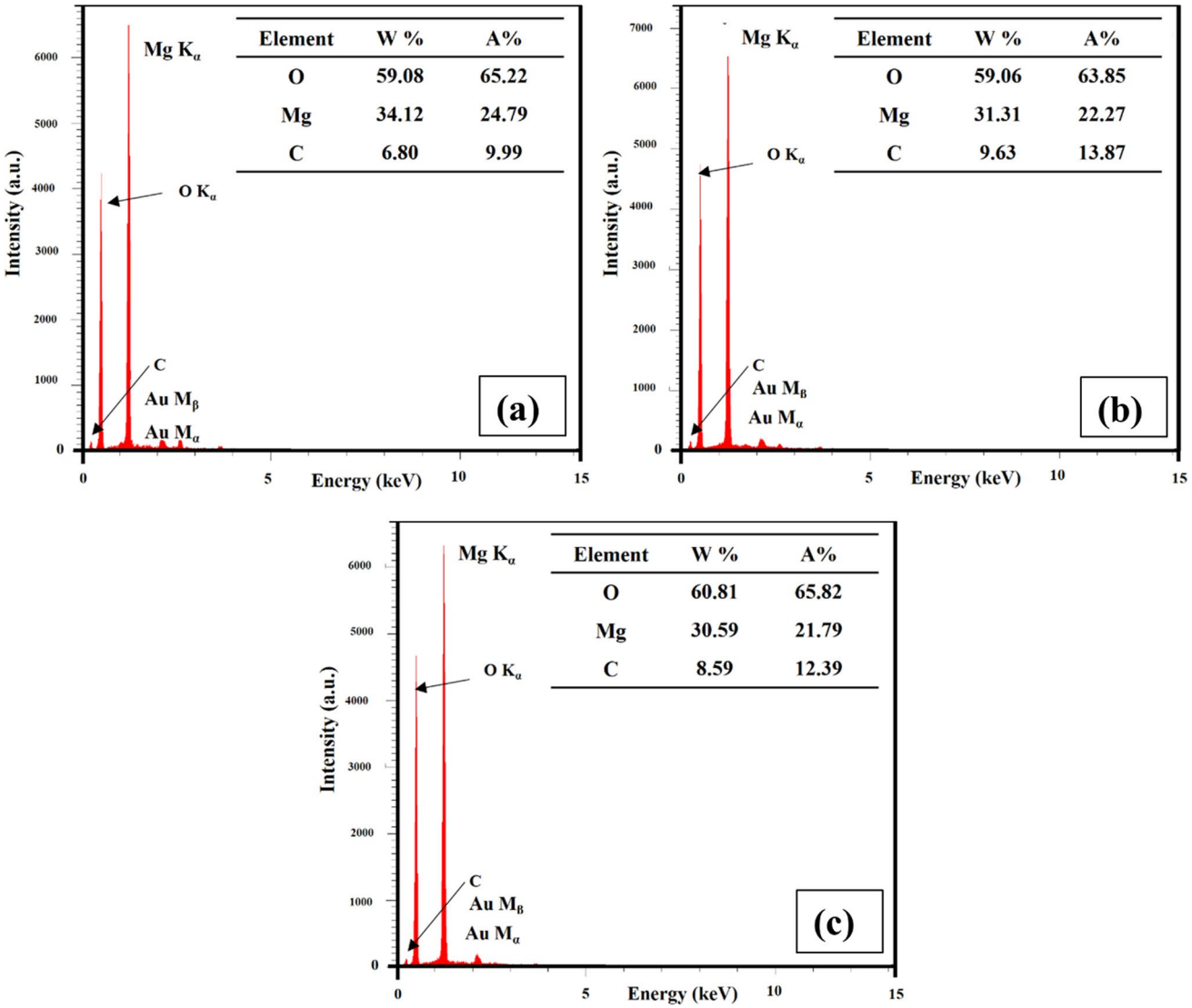

Fig. 4 EDS spectra and corresponding elemental analysis of $Mg(OH)_2$ nanostructures prepared via ultrasonic irradiation under different irradiation powers: **a** MH-100; **b** MH-200; and **c** MH-350

pores (i.e. plates or edged particles such as cubes), whose size and/or shape are non-uniform [66]. The average pores size distributions of the synthesized $Mg(OH)_2$ samples were determined by the Barrett–Joyner–Halenda (BJH) method that uses the desorption branch, as shown in Fig. 7 (inset). The surface area of the specimens was measured using the BET and Langmuir methods. The theoretical particle sizes were estimated from the surface area (i.e. assuming spherical particles) using the following relation:

$$D_{BET} = \left(\frac{6000}{\rho * S}\right) \quad (4)$$

where D_{BET}, ρ, and S are the equivalent particle diameter (nm), the density of the sample (g cm^{-3}), and the specific surface area (m^2 g^{-1}), respectively. The pore structure parameters of the $Mg(OH)_2$ samples are listed in Table 4. An increase in D_{BET} was observed with an increase in the power of ultrasonic waves. Increasing the ultrasonic radiation intensity raised the surface energy of the particles, which was linked with breaking of the particles in the early stages of synthesis, resulting in their agglomeration and associated increase in particle sizes.

The increase in irradiation power also influenced the pore size distribution. Accordingly, at higher power values,

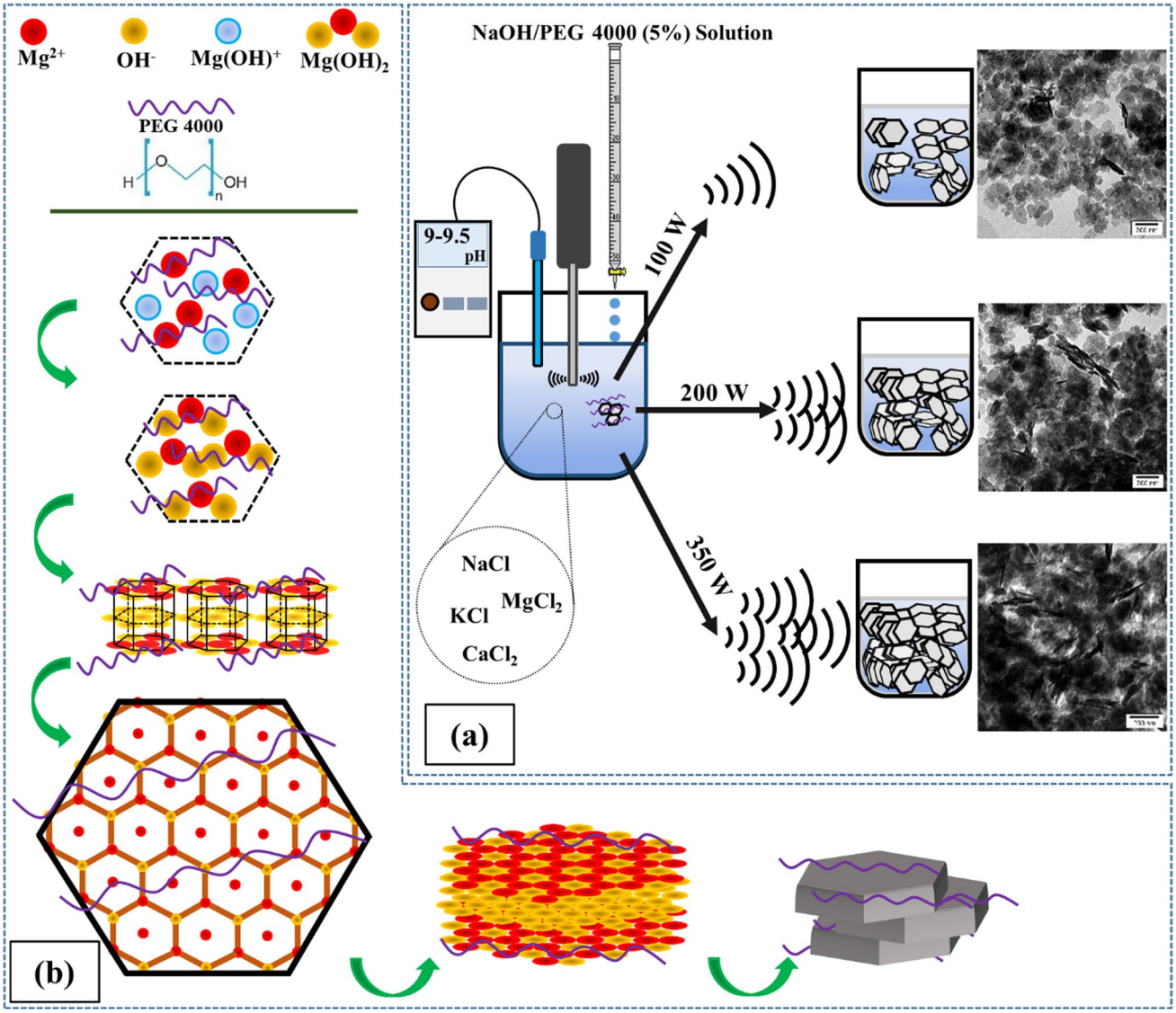

Fig. 5 **a** Schematic representation of the formation of $Mg(OH)_2$ nanoflakes and effect of ultrasound irradiation, **b** The $Mg(OH)_2$ crystal growth mechanism by surfactant assisted sonochemical method using brine

a shift in the pore size distribution towards larger values was observed. Alternatively, both the specific surface areas and pore volumes of the $Mg(OH)_2$ samples significantly decreased by rising irradiation power. The maximum surface area was revealed by the MH-100 sample as 116.30 $m^2\ g^{-1}$, with a corresponding pore volume of 0.57 $cm^3\ g^{-1}$, which was obtained under ultrasonic irradiation at a power of 100 W. While 100 W revealed samples with the lowest average pore and particle size, the nanostructures of all samples consisted of large mesopores with pore sizes of less than 50 nm. Differing from others, the defining feature of the MH-100 sample was the presence of smaller mesopores between 4 and 10 nm, whereas the mesopores for MH-200 and MH-350 samples disappeared or merged due to the aggregation of nanoplates and reached 2–4 nm, which were consistent with FESEM and TEM observations.

3.4 Thermal and optical properties

The thermal behavior of MH samples was investigated using TG–DTA and DSC analysis and obtained results are presented in Fig. 8 and Table 5. The TG–DTA and DSC patterns of MH nanostructures indicate that the thermal decomposition of all as-synthesized consists of two stages. First, an endothermic peak (before 200 °C) is ascribed to the removal of water and some PEG. Second, another endothermic peak centered (before 400 °C) corresponds to the complete removal of PEG, decomposition of MH nanostructures,

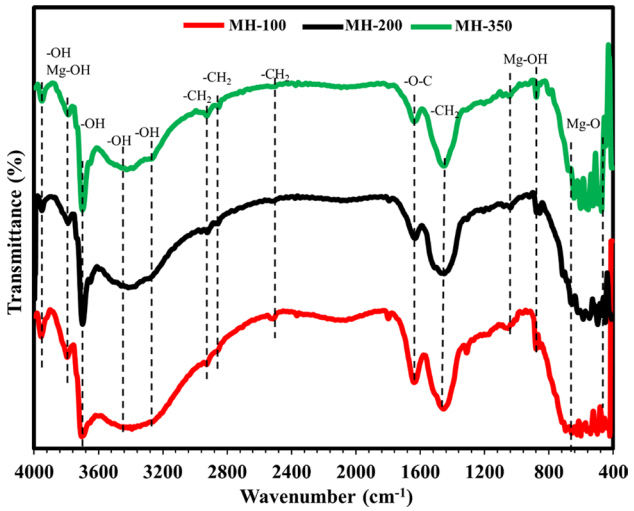

Fig. 6 FTIR spectra of $Mg(OH)_2$ nanostructures prepared via ultrasonic irradiation under different irradiation powers

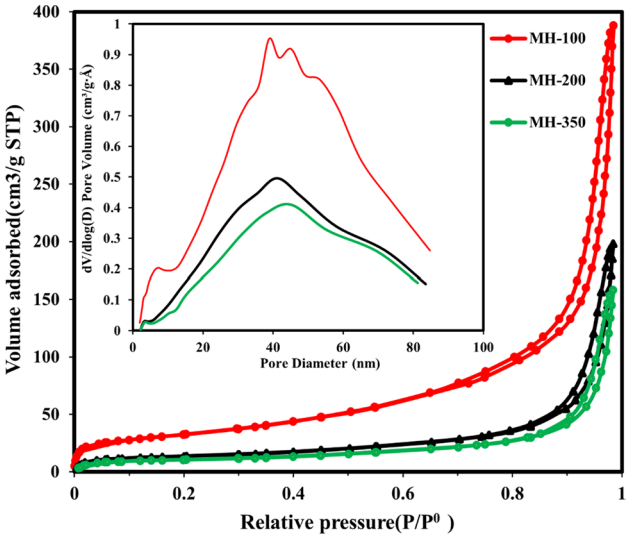

Fig. 7 N_2 adsorption–desorption isotherms of as-synthesized $Mg(OH)_2$ nanopowders; inset: pore size distribution deduced from desorption branch

and transformation to MgO nanostructures according to the following reaction [25]:

$$Mg(OH)_2 \rightarrow MgO + H_2O \quad (5)$$

The TG curves indicated that the weight losses of samples in the first stage were approximately 4.5%, 6.6%, and 6.8%, while in the second stage, final weight losses were 15.3%, 16.6%, and 17% for MH-100, MH-200, and MH-350, respectively. Based on DTA results, the transformation temperature (T_t) of $Mg(OH)_2$ to nanostructures MgO was 375 °C, 388 °C, and 394 °C, respectively. The final decomposition temperature for $Mg(OH)_2$ nanostructures in this study was lower than the reported temperature in the literature [9]. According to the obtained results (Table 5), increasing the power of ultrasonic waves leads to an increase in the percentage of mass loss in stages 1 and 2 and an enhancement in the transformation temperature of $Mg(OH)_2$ into MgO.

Table 4 Results of N_2-adsorption/desorption analysis of $Mg(OH)_2$ nanopowders

Sample	Specific surface area (m^2/g)		Pore volume (cm^3/g)	Average pore size (nm)	Particle size (D_{BET}) (nm)
	S_{BET}	$S_{Langmuir}$			
MH-100	116.30	156.63	0.57	16.59	21.76
MH-200	46.19	67.48	0.29	21.22	54.69
MH-350	35.40	52.79	0.24	23.37	71.51

The reason for this behavior can be attributed to an increase in the agglomeration of particles, an increase in temperature, and the required energy to convert $Mg(OH)_2$ into MgO.

The optical specifications of the samples were studied by using UV–Vis DRS. Figure 9 indicates the absorption

Table 3 FTIR spectroscopy data for $Mg(OH)_2$ nanostructures prepared via ultrasonic irradiation

Peak position (cm^{-1})	Intensity	Peak mode(s)	References
430–520	Sharp and weak	Tensile vibration of Mg-O	[55, 56]
540–600	Small and sharp	Deformation vibration of water and stretching vibration of Mg-OH	[57, 58]
880, 1043	Small	Asymmetric tensile vibrations of C–O–C in PEG	[53, 59]
1398	Strong and wide	Shear-blending vibrations of CH_2 in PEG	[60]
1627	Wide and weak	Tensile vibrations of C-O in PEG	
2503, 2852, 2927	Small and weak	Tensile vibrations of CH_2 in PEG	[53, 59, 61]
3260, 3440	Board and weak	Tensile vibration of OH in water and PEG	
3699	Strong and sharp	Tensile vibration of OH in $Mg(OH)_2$	[61, 62]
3743, 3948	Small and weak	Tensile vibration of OH in water and Mg-OH	[63, 64]

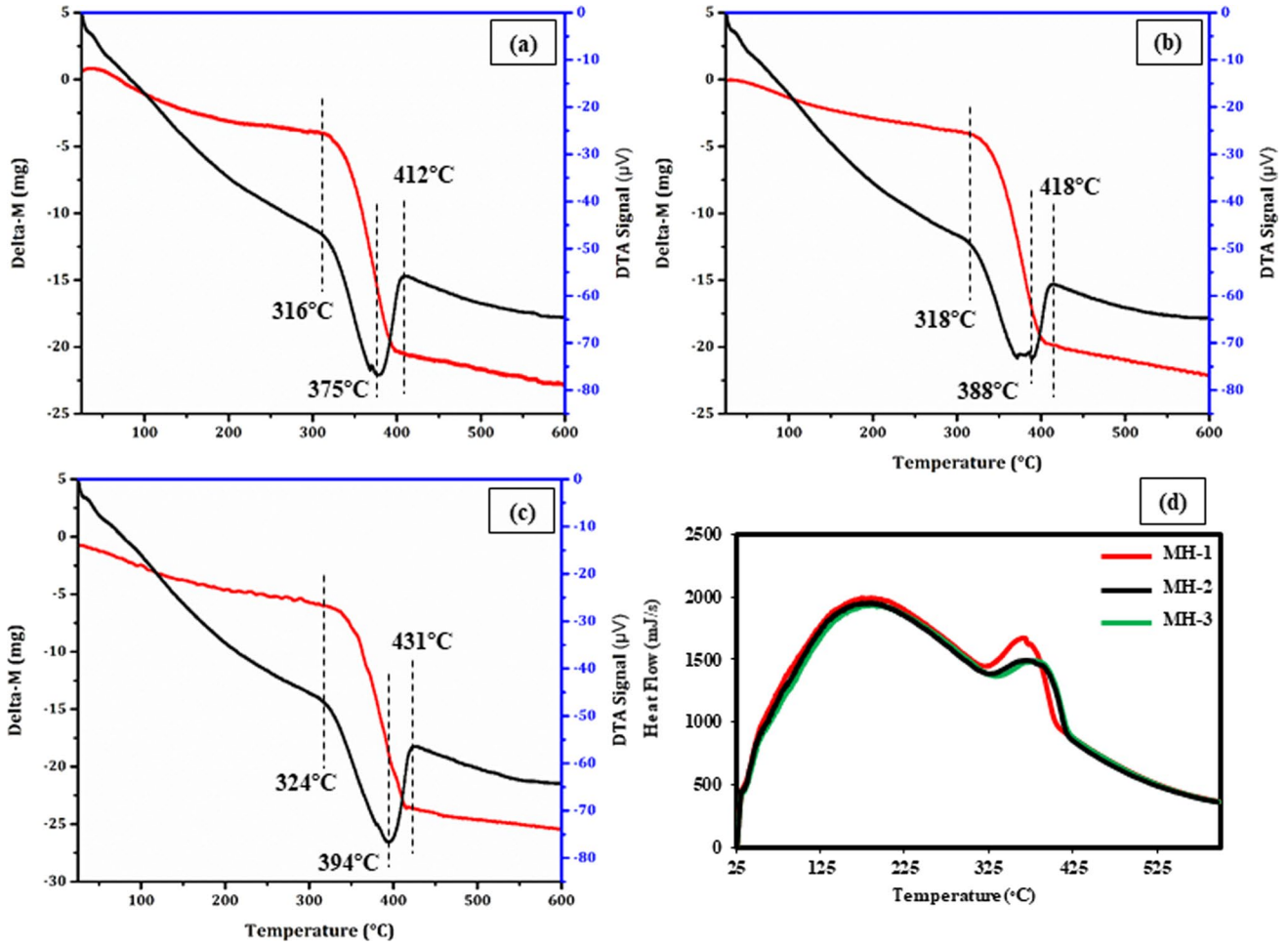

Fig. 8 **a–c** TG–DTA patterns, and **d** DSC curves of $Mg(OH)_2$ nanostructures prepared via ultrasonic irradiation under different irradiation powers

Table 5 Extracted data from TG–DTA and DSC profiles of as-synthesized $Mg(H)_2$ samples

Sample	TGA				DSC		DTA
	T_i (°C)	T_f (°C)	Weight loss 1 (%)	Weight loss 2 (%)	T_{p1} (°C)	T_{p2} (°C)	T_t (°C)
MH-100	316	412	4.5	15.3	184.6	365.2	375
MH-200	318	418	4.8	16.6	187.3	373.7	388
MH-350	324	431	6.6	17.0	188.7	382.1	394

and transmittance spectra corresponding to $Mg(OH)_2$ samples synthesized under different ultrasound irradiation powers. As shown by the absorption and transmittance spectra of all samples, these spectra were divided into two regions: (a) the low absorption and low passage region with a wavelength of < 240 nm, known as the absorption edge (i.e. due to the excitation of four-fold coordinated O^{2-} anions in the edges and corners), and (b) the lower absorption and higher transmittance region with a wavelength of > 240 nm and a low change slope. The absorption rate in all $Mg(OH)_2$ samples increased towards shorter wavelengths (i.e. ultraviolet). The appearance of these peaks in the UV region was related to the transition of the band to band in the band gap zone [67]. An initial sharp reduction in the absorbance with an increase in wavelength was followed by almost a constant absorption coefficient, indicating the monotony in the size of as-synthesized $Mg(OH)_2$ nanoplates [68]. The appearance of a new absorption region in the 240–340 nm range (i.e. with a 290 nm absorption edge) in the MH-350 sample

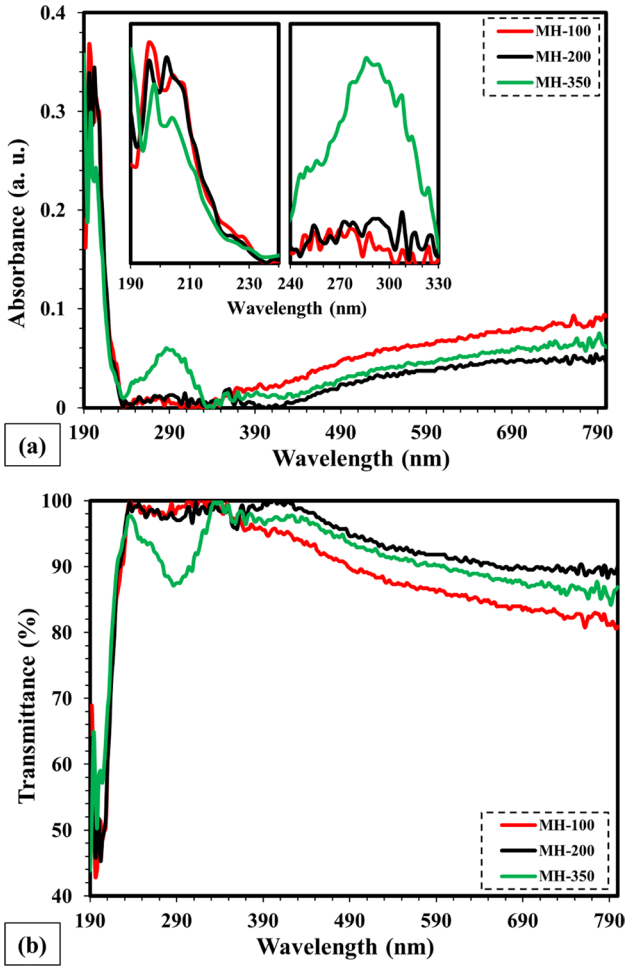

Fig. 9 UV–vis **a** absorption and **b** transmittance spectra of $Mg(OH)_2$ nanostructures prepared via ultrasonic irradiation under different irradiation powers

could be associated with the excitation of three-fold coordinated O^{2-} anions in the edges and corners [69]. Also, this peak could be due to a quantum confinement effect or morphological impacts on $Mg(OH)_2$ crystals with many active sites and an increase in the surface electric charge of $Mg(OH)_2$ nanoplates that could have altered the exciton formation upon irradiation [22, 70].

The optical band energy gap (E_g) is an important parameter that is used in the design and manufacture of semiconductors and dielectric materials [71]. E_g can be derived from the relation of the void that demonstrates the dependence of the absorption coefficient (α) on the photon energy (hυ), based on Eq. 6 [72]:

$$(\alpha h\nu)^2 = A\left(h\nu - E_g\right) \tag{6}$$

where A is a material-dependent constant, h is Planck's constant, and ν is the photon frequency. Accordingly, the direct band gap energy values of $Mg(OH)_2$ samples were determined by Tauc plot and plotting $(\alpha h\upsilon)^2$ vs. photon energy (hυ) by extrapolating the linear part of the Tauc's plot, as shown in Fig. 10. The Eg values of MH-100, MH-200, and MH-350 samples were estimated as 5.80 eV, 5.75 eV, and 5.7 eV, respectively. The observed difference can be attributed to the changing particle size with the increase in ultrasound irradiation power. In the case of a reduction in the size of the nanoparticles in the valence and conduction bands discreet atomic-like energy levels occur [73]. The spacing between the electronic levels and bind gap energy increases with decreasing the particle size which statement is fully consistent with the results in this study. This phenomenon Wang et al. [74] explain with the surface/volume ratio fluctuation and the surface atoms' relaxation effects. This minor difference in the bind gap energy may be also due to a decrease in energy level in $Mg(OH)_2$ nanoflakes because of the relative reduction of internal stress, the surface polarity of $Mg(OH)_2$, and the formation of a stable structure. Based on the results of this study, the $Mg(OH)_2$ nanoflakes can be a good candidate material for applications in photocatalysis, optoelectronics, photonics, and microelectronics.

4 Conclusion

In this work, $Mg(OH)_2$ nanoflakes have been successfully fabricated using a simple surfactant-assisted sonochemical method at different irradiation powers of 100, 200, and 350 W. Morpho-structural studies indicated that sonochemical synthesis with radiation power higher than 100 W, greatly increases the crystallites and particles size and intensifies the formation of agglomerations of $Mg(OH)_2$ nanoflakes. The agglomeration of $Mg(OH)_2$ particles at higher irradiation powers were caused by fast nucleation and growth in the precipitation process. On the other hand, FTIR analysis indicated that an increase in irradiation power did not affect the structure of $Mg(OH)_2$ nanoflakes. The BET results indicated a significant decrease in the surface area with the increase in the power irradiation in the samples together with the increase in the average pore size of the samples. Also, the TG–DTA/DSC results indicated that the increase in power irradiation of ultrasound waves increases the decomposition temperature range of $Mg(OH)_2$ nanoflakes and the phase transformation temperature of $Mg(OH)_2$ to MgO. The UV–Vis spectrum proved that the optical band gap energy increased from 4.70 to 4.80 eV with the increasing power of irradiation from 100 to 350 W. Therefore, the band gap in $Mg(OH)_2$ nanoflakes may be tuned by controlling crystallite size and hence by controlling the power of irradiation in the sonochemical method. The band gap tuning of $Mg(OH)_2$

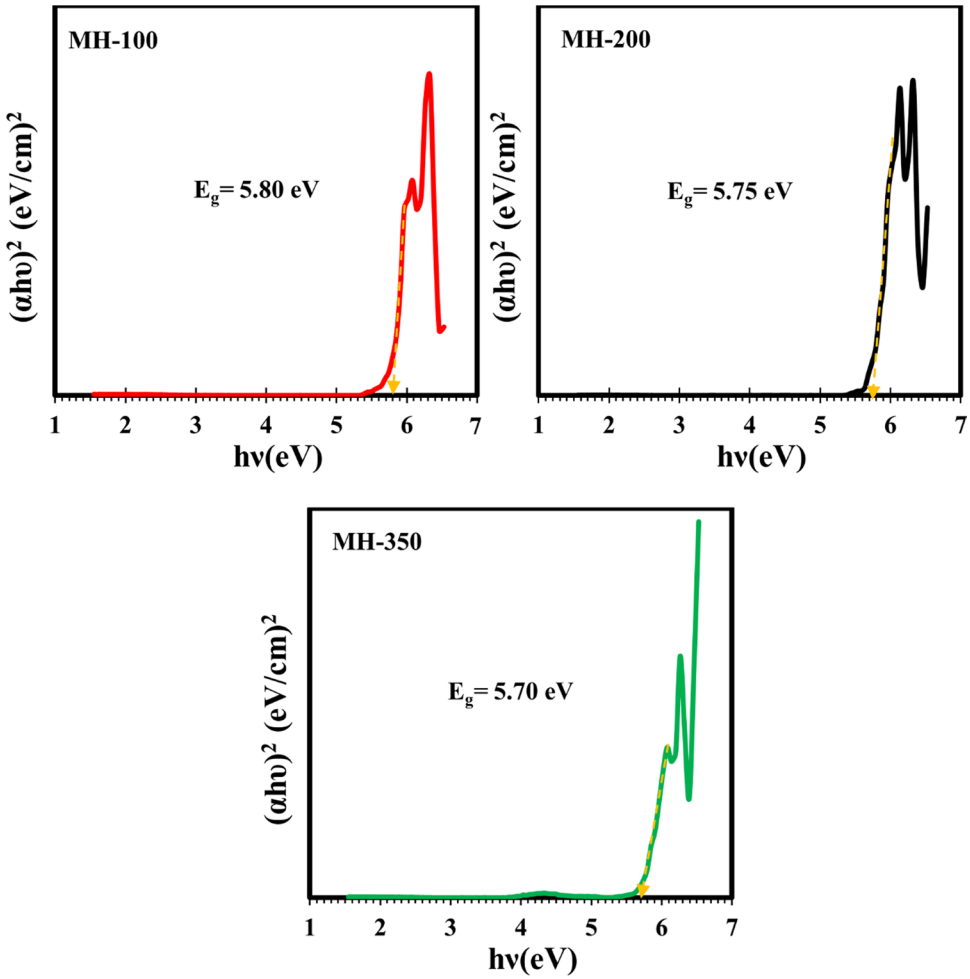

Fig. 10 Band gap of $Mg(OH)_2$ nanostructures prepared via ultrasonic irradiation under different irradiation powers

nanostructures in the ultraviolet zone illustrates its potential applications in optoelectronic and photocatalytic applications. Also, the presence of porosity in the synthesized $Mg(OH)_2$ nanostructures makes it possible to use them in different fields such as gas adsorption and storage, wastewater treatment, electrochemical applications, catalysis, and drug delivery.

Author contributions Sadegh Yousefi performed investigation; writing—original draft and methodology; formal analysis; conceptualization. Behrooz Ghasemi performed writing—review and editing; formal analysis; conceptualization; supervision. Maria Plamenova Nikolova performed writing—review and editing; visualization; validation. Cise Unluer performed writing—review and editing; supervision.

Data availability Experimental and analysis data can be made available on request.

Declarations

Conflict of interest The authors declare that they have no conflict of interest.

References

1. J.L. Booster, A. Van Sandwijk, M.A. Reuter, Miner. Eng. **16**, 273 (2003)
2. S. Wang, X. Yang, Y. Li, B. Gao, S. Jin, R. Yu, Y. Zhang, Y. Tang, Colloidal. J. Colloid Interface Sci. **607**, 992 (2022)
3. A.A. Hanna, A.S. Abdelmoaty, M.A. Sherief, J. Chem. **2019**, 1 (2019)
4. H. Kim, J. Singh, Y.N. Yun, M. Sohail, T.W. Kim, J.Y. Lee, W. Choi, D. Kim, A.C.S. Appl, Nano Mater. **3**, 2207 (2020)
5. Z. Rajabimashhadi, R. Naghizadeh, A. Zolriasatein, C. Esposito Corcione, Nanomaterials **13**, 454 (2023)
6. R. Eivazzadeh-Keihan et al., ACS Appl. Mater. Interfaces **13**, 33840 (2021)
7. F. Al-Hazmi, A. Umar, G.N. Dar, A.A. Al-Ghamdi, S.A. Al-Sayari, A. Al-Hajry, S.H. Kim, R.M. Al-Tuwirqi, F. Alnowaiserb, F. El-Tantawy, J. Alloys Compd. **519**, 4 (2012)
8. B.J. Wang, X.H. Li, X.L. Cai, W.Y. Yu, L.W. Zhang, R.Q. Zhao, S.H. Ke, J. Phys. Chem. C **122**, 7075 (2018)
9. P. Yadav, R. Saini, A. Bhaduri, Environ. Sci. Pollut. Res. **30**, 71439 (2023)
10. N. Ponomarev, O. Pastushok, E. Repo, B. Doshi, M. Sillanpää, A.C.S. Appl, Nano Mater. **2**, 5492 (2019)

11. O. Falyouna, K. Bensaida, I. Maamoun, U.P.M. Ashik, A. Tahara, K. Tanaka, N. Aoyagi, Y. Sugihara, O. Eljamal, J. Clean. Prod. **342**, 130949 (2022)
12. K. Dharamalingam et al., Biomass Convers. Biorefinery **13**, 13539 (2023)
13. D. Karthigaimuthu, S. Ramasundaram, P. Nisha, B. Arjun Kumar, J. Sriram, G. Ramalingam, P. Vijaibharathy, T.H. Oh, T. Elangovan, Chemosphere **308**, 136406 (2022)
14. K. Dharmalingam, V. Gurudevan, G. Dhanasekaran, D. Sekar, R. Gopal, D. Alshamsi, E. Thangavel, S. Sambasivam, J. Mater. Res. **39**, 231 (2024)
15. C. Henrist, J.-P. Mathieu, C. Vogels, A. Rulmont, R. Cloots, J. Cryst. Growth **249**, 321 (2003)
16. D. Zhang, P. Zhang, S. Song, Q. Yuan, P. Yang, X. Ren, J. Alloys Compd. **612**, 315 (2014)
17. X. Li, T. Shi, P. Chang, H. Hu, J. Xie, Y. Liu, Powder Technol. **260**, 98 (2014)
18. A. Sierra-Fernandez, L.S. Gomez-Villalba, O. Milosevic, R. Fort, M.E. Rabanal, Ceram. Int. **40**, 12285 (2014)
19. J. Jeevanandam, Y.S. Chan, M.K. Danquah, Part. Sci. Technol. **38**, 573 (2020)
20. X. Liu, C. Liao, L. Lin, H. Gao, J. Zhou, Z. Feng, Z. Lin, Surfaces Interfaces **21**, 100701 (2020)
21. H. Yan, J. Wu, X. Zhang, Y. Zhang, L. Wei, X. Liu, B. Xu, J. Mater. Res. **22**, 2544 (2007)
22. P. Yadav, A. Bhaduri, Ionics **30**, 529 (2024)
23. W. Fan, S. Sun, X. Song, W. Zhang, H. Yu, X. Tan, G. Cao, J. Solid State Chem. **177**, 2329 (2004)
24. V. Sirota, V. Selemenev, M. Kovaleva, I. Pavlenko, K. Mamunin, V. Dokalov, M. Yapryntsev, Preparation of crystalline $Mg(OH)_2$ nanopowder from serpentinite mineral. Int. J. Min. Sci. Technol. **28**, 499 (2018)
25. J. Wu, H. Yan, X. Zhang, L. Wei, X. Liu, B. Xu, Magnesium hydroxide nanoparticles synthesized in water-in-oil microemulsions. J. Colloid Interface Sci. **324**, 167 (2008)
26. A. Pilarska, E. Markiewicz, F. Ciesielczyk, T. Jesionowski, The influence of spray drying on the dispersive and physicochemical properties of magnesium oxide. Dry. Technol. **29**, 1210 (2011)
27. S. Utamapanya, K.J. Klabunde, J.R. Schlup, Nanoscale metal oxide particles/clusters as chemical reagents. Synthesis and properties of ultrahigh surface area magnesium hydroxide and magnesium oxide. Chem. Mater. **3**, 175 (1991)
28. L. Sun, H. He, C. Liu, Z. Ye, Local super-saturation dependent synthesis of MgO nanosheets. Appl. Surf. Sci. **257**, 3607 (2011)
29. M.A. Alavi, A. Morsali, Syntheses and characterization of $Mg(OH)_2$ and MgO nanostructures by ultrasonic method. Ultrason. Sonochem. **17**, 441 (2010)
30. S. Yousefi, B. Ghasemi, Micro Nano Lett. **14**, 1019 (2019)
31. H. Wu, B. Luo, C. Gao, L. Wang, Y. Wang, Q. Zhang, J. Dispers. Sci. Technol. **41**, 585 (2020)
32. A.A. Pilarska, Ł Klapiszewski, T. Jesionowski, Powder Technol. **319**, 373 (2017)
33. M. Tamiji, A.R. Ahmadian-Fard-Fini, M. Behzadi, D. Ghanbari, J. Nanostructures **11**, 31 (2021)
34. P. Chen, Y. Wang, S. He, P. Wang, Y. Xu, L. Zhang, Adv. Mater. Sci. Eng. **2020**, 1 (2020)
35. H. Chen, E. Bao, H. Sun, X. Ren, X. Han, Y. Wang, Z. Zhang, C. Luo, C. Xu, J. Colloid Interface Sci. **664**, 117 (2024)
36. M. Salavati-Niasari, G. Hosseinzadeh, F. Davar, J. Alloys Compd. **509**, 4098 (2011)
37. A. Numan, N. Duraisamy, F. Saiha Omar, D. Gopi, K. Ramesh, S. Ramesh, Prog. Nat. Sci. Mater. Int. **27**, 416 (2017)
38. S.B. Devi, S. Sekar, K. Kowsuki, T. Maiyalagan, V. Preethi, R. Nirmala, S. Lee, R. Navamathavan, Int. J. Hydrogen Energy **47**, 40349 (2022)
39. J. Sarmet, C. Taviot-Gueho, R. Thirouard, F. Leroux, C. Douard, I. Gaalich, T. Brousse, G. Toussaint, P. Stevens, Cryst. Growth Des. **23**, 2634 (2023)
40. B. Aljafari, S.N. Kanimozhi, J.J. Wu, S. Anandan, Inorg. Chem. Commun. **159**, 111748 (2024)
41. M.S.Y. Parast, A. Morsali, Ultrason. Sonochem. **18**, 375 (2011)
42. M. Mousavi-Kamazani, S. Zinatloo-Ajabshir, M. Ghodrati, J. Mater. Sci. Mater. Electron. **31**, 17332 (2020)
43. S. Alinavaz, M. Ghiyasiyan-Arani, E.A. Dawi, M. Salavati-Niasari, Int. J. Hydrogen Energy **48**, 28424 (2023)
44. H. Guo, S. Fu, G. Xue, F. Lai, and T. Liu, Small Sci. 2300150 (2023). https://doi.org/10.1002/smsc.202300150
45. O. Baidukova, E.V. Skorb, Ultrason. Sonochem. **31**, 423 (2016)
46. S. Yousefi, B. Ghasemi, M. Tajally, Appl. Phys. A **126**, 641 (2020)
47. S. Yousefi, B. Ghasemi, M. Tajally, A. Asghari, J. Alloys Compd. **711**, 521 (2017)
48. X. Ma, H. Ma, X. Jiang, Z. Jiang, Mater. Res. Bull. **56**, 113 (2014)
49. C.H.S.S.P. Kumar, R. Pandeeswari, B.G. Jeyaprakash, J. Alloys Compd. **602**, 180 (2014)
50. X. Cao, H. Zhao, X. Liu, H.H. Luo, R. Liu, J. Cryst. Growth **550**, 125841 (2020)
51. D.K. Chanda, P.S. Das, A. Samanta, A. Dey, A.K. Mandal, K. Das Gupta, T. Maity, A.K. Mukhopadhyay, Ceram. Int. **40**, 11411 (2014)
52. S. Yousefi, B. Ghasemi, M.P. Nikolova, Appl. Phys. A **127**, 549 (2021)
53. A. Pilarska, M. Wysokowski, E. Markiewicz, T. Jesionowski, Powder Technol. **235**, 148 (2013)
54. M. Nasir, J. Lei, W. Iqbal, J. Zhang, Appl. Surf. Sci. **364**, 446 (2016)
55. D. An, X. Ding, Z. Wang, Y. Liu, Colloids Surfaces A Physicochem. Eng. Asp. **356**, 28 (2010)
56. S. Yousefi, B. Ghasemi, M.P. Nikolova, J. Clust. Sci. **33**, 2197 (2022)
57. A. Umar, F. Al-Hazmi, G.N. Dar, S.A. Zaidi, R.M. Al-Tuwirqi, F. Alnowaiserb, A.A. Al-Ghamdi, S.W. Hwang, Sensors Actuat. B Chem. **166–167**, 97 (2012)
58. S. Yousefi, B. Ghasemi, Res. Chem. Intermed. **47**, 2029 (2021)
59. A. Pilarska, M. Nowacka, K. Pilarski, Physicochem. Probl. Miner. Process. **49**, 701 (2013)
60. P. Tripathi, A. Ahmed, T. Ali, and M. Obaidurrahman, in *AIP Conference Proceedings*, Vol. 1731 (2016), p. 050067.
61. S.-Y. Wang, G.-M. Li, W. Xu, C. Liu, L. Dai, H.-C. Zhu, Res. Chem. Intermed. **42**, 2661 (2016)
62. R. Kurosawa, M. Takeuchi, J. Ryu, J. Phys. Chem. C **125**, 5559 (2021)
63. A. Kumar, J. Kumar, J. Phys. Chem. Solids **69**, 2764 (2008)
64. M.S. Hamdy, N.S. Awwad, A.M. Alshahrani, Mater. Des. **110**, 503 (2016)
65. J. Zhou, W. Wang, Y. Cheng, Z. Zhang, Integr. Ferroelectr. **137**, 18 (2012)
66. F. Meshkani, M. Rezaei, Powder Technol. **199**, 144 (2010)
67. A.A. Al-Ghamdi, F. Al-hazmi, F. Alnowaiser, R.M. Al-Tuwirqi, A.A. Al-Ghamdi, O.A. Alhartomy, F. El-Tantawy, F. Yakuphanoglu, J. Electroceramics **29**, 198 (2012)
68. A. Sharma, S. Arya, B. Singh, Prerna, A. Tomar, S. Singh, R. Sharma, Integr. Ferroelectr. **205**, 14 (2020)
69. N.C.S. Selvam, R.T. Kumar, L.J. Kennedy, J.J. Vijaya, J. Alloys Compd. **509**, 9809 (2011)
70. R. Bhargava, S. Khan, Adv. Powder Technol. **28**, 2812 (2017)
71. R. Al-Gaashani, S. Radiman, Y. Al-Douri, N. Tabet, A.R. Daud, J. Alloys Compd. **521**, 71 (2012)
72. M.A. Almessiere, Y. Slimani, A.D. Korkmaz, N. Taskhandi, M. Sertkol, A. Baykal, S.E. Shirsath, Ercan, B. Ozçelik, Ultrason. Sonochem. **58**, 104621 (2019)

73. E.O. Chukwuocha, M.C. Onyeaju, T.S.T. Harry, World J. Condens. Matter Phys. **02**, 96 (2012)
74. Y. Wang, G. Ouyang, L.L. Wang, L.M. Tang, D.S. Tang, C.Q. Sun, Chem. Phys. Lett. **463**, 383 (2008)